FERMILAB
JUN 12 1995
LIBRARY
IFA-95-12
31
Fermilab Library
0 1160 0047117 1

IFA - 95/12 Mar. 1995

AARHUS-ASTRO-1995-06 ISSN 0906-3870

A GRADIENT IN THE SURFACE BRIGHTNESS FLUCTUATIONS OF NGC 3379

Marianne Sodemann and Bjarne Thomsen

Inst. of Physics and Astronomy
University of Aarhus
DK-8000 Aarhus C
Denmark

To appear in The Astronomical Journal, July 1995

Submitted to The Astronomical Journal

A Gradient in the Surface Brightness Fluctuations of NGC 3379 [1]

Marianne Sodemann and Bjarne Thomsen
Institute of Physics and Astronomy, University of Aarhus, DK-8000 Aarhus C.
Electronic mail: ms@obs.aau.dk, bt@obs.aau.dk

ABSTRACT

We present an investigation of the radial behavior of the surface brightness fluctuations of the standard elliptical galaxy NGC 3379, and we demonstrate that it is possible to measure radial changes accurately. Our results are based on a thorough procedure, which takes into account that the unwanted point sources, such as foreground stars, background galaxies and globular clusters, are located in a background of varying amounts of luminosity and photon fluctuations. Our reduction procedure leaves no systematic effects due to the varying detection threshold of point sources, and we arrive at a significant radial gradient in the surface brightness fluctuations $\Delta\bar{m}_I/\Delta \log R = -0.29 \pm 0.08$. If our broad-band surface brightness profile of NGC 3379 in I is combined with a corresponding profile in B taken from the literature, the radial behavior of $\bar{m}_I$ may be expressed as $\Delta\bar{m}_I/\Delta(B-I) = 1.9 \pm 0.5$. The weighted mean of the measured fluctuation magnitudes is $\bar{m}_I = 28.67 \pm 0.04$. Our results have implications on the distance measurements based on surface brightness fluctuations and the discussion of the degenerate effects of age and metallicity on stellar populations of elliptical galaxies. The linear relationship between $\bar{m}_I$ and $B-I$ establishes an empirical calibration, which is needed for the distance measurements based on surface brightness fluctuations. The slope of the calibration obtained for NGC 3379 seems to be in agreement with the slope achieved earlier by others for Local Group galaxies and the Fornax and Eridanus clusters. The fluctuation magnitude $\bar{m}_I$ proves to be a sensitive indicator for radial changes in the underlying stellar population. However, the correlation between $\bar{m}_I$ and $B-I$ together with state-of-the-art synthesized models indicates that these two observables do not give independent information on the underlying stellar population.

Subject headings: galaxies: ellipticals — galaxies: individual (NGC 3379)

---

[1] Based on observations made at the European Southern Observatory, La Silla, Chile.

1. Introduction

From groundbased observations of galaxies it is possible to obtain information on both the mean and the variance of the stellar luminosity function for elliptical galaxies. The method of surface brightness fluctuations was introduced in 1988 by Tonry & Schneider as a new technique for measuring extra-galactic distances. It is now a well-established and frequently applied distance indicator (see e.g. Tonry *et al.* 1990, Tonry 1991, Jacoby *et al.* 1992, Dressler 1993, Simard & Pritchet 1994 and Pahre & Mould 1994). As emphasized by Tonry & Schneider (1988) the variance of the galaxy light ought to give some additional information to the list of broad-band colors and spectral line indices obtained from the mean of the galaxy light. This new information may be expected, due to the fact that the variance of the galaxy light is based on a different weighting of the stars in the HR-diagram of a galaxy than is the integrated light. Both approaches to the applications of luminosity fluctuations, distance determination and investigation of stellar population, are affected by our results.

The surface brightness fluctuations (SBF) are due to the counting statistics of the stars contributing the flux in each of the pixels covering a galaxy. A simplified presentation of some of the properties of SBF is given in the following. The complete introduction is found in Tonry & Schneider (1988). Let N be the number of stars per pixel, each with flux $\bar{f}$. Then the galaxy flux per pixel is $g = \bar{f}N$, and the average galaxy flux per pixel is $\bar{g} = \bar{f}\bar{N}$. Due to the Poisson statistics of the stars the variance of the galaxy flux is $\sigma_{\rm L}^2 = \bar{f}^2\bar{N}$. This implies that $\sigma_{\rm L}^2 = \bar{f}\bar{g}$, which expresses the fact that the luminosity fluctuations scale with the signal from the galaxy. According to the above, the normalized luminosity fluctuations are expressed as the flux $\bar{f} \equiv \tilde{\sigma}_{\rm L}^2 = \sigma_{\rm L}^2/\bar{g}$ measured in ADUs, or as the magnitude $\bar{m}$ or $\bar{I}$. This flux weighted mean flux $\bar{f}$ is dominated by the light from the giant branch stars.

The root mean square (rms) luminosity fluctuations emerge when the average galaxy flux per pixel is subtracted from the image. The basis of the SBF method is the straightforward way to measure the variance $\sigma_{\rm L}^2$. Sources of white noise (photon noise and readout noise) separate from the luminosity fluctuations by a Fourier transform, due to the fact that white noise will show up with a white power spectrum, whereas the luminosity fluctuations will appear with the point-spread function (PSF) impressed upon them. In contrast to this relatively simple separation comes the troublesome task of eliminating all unwanted contributions to the fluctuation signal, that is, contributions from foreground stars, background galaxies and globular clusters of the target galaxy, which also have the PSF impressed upon them. Because these distracting point sources are located in differing amounts of luminosity and photon fluctuations, it is a delicate task to correct for their presence. The contribution to the variance from unidentified point sources must carefully be

taken care of, especially when dealing with the radial changes of the luminosity fluctuations.

The well-observed luminosity standard E0 galaxy NGC 3379 was picked out as a 'study-case' for our analysis. We have established a reliable procedure, which takes into account the varying amplitude of luminosity and photon fluctuations within the image of a galaxy. We describe our reduction procedure in detail and we present a significant radial gradient in the I-band luminosity fluctuations of this closest normal elliptical NGC 3379. The radial variation in $\bar{m}_I$ is intrinsic to the galaxy and is caused by variations in the underlying stellar population, either due to differencies in metallicity or age, or both. The broad-band color $B-I$ correlates linearly with $\bar{m}_I$ within NGC 3379. The tight correlation between $\bar{m}_I$ and $B-I$ is of vital importance to the SBF distance determinations, because it makes it possible to calibrate the radial dependence of the luminosity fluctuations. We compare our results for NGC 3379 with the results for the Local Group galaxies and the Fornax and Eridanus clusters (Tonry 1991).

Worthey (1994) has presented a large sample of detailed models for intermediate and old stellar populations with the hope to disentangle the degeneration of age and metallicity effects. The models assume one metallicity ($-2 < [\mathrm{Fe/H}] < 0.5$) and one age (between 1.5 and 17 Gyr) for the whole population. The work includes a wide variety of observables, such as fluctuation magnitudes and colors, in addition to more traditional indicators like broad-band magnitudes and spectral line indices. These models imply gradients in the I-band fluctuation magnitude, which we compare with our results and observations by others. The radial changes in the stellar population constituting NGC 3379 have an explicit influence on the I-band luminosity fluctuations, which gives rise to the measurable radial gradient in $\bar{m}_I$. Our preliminary results on SBF were presented in Thomsen & Sodemann (1993) and Sodemann & Thomsen (1994b).

2. Observations and Reductions

Our data were collected on 1993 April 25 – 26 with the 3.5 m NTT (New Technology Telescope) at the European Southern Observatory, La Silla, Chile. The instrument was the SUperb Seeing Imager (SUSI) with a TEK-1024 CCD, 24 μm per pixel, readout noise 2.3 ADU and gain 3.3 e^- per ADU. The image scale was 0.″134 per pixel. The data are the same as described by Sodemann & Thomsen (1994a) (hereafter ST). In ST we presented our galaxy-fitting routine, which is capable of fitting incomplete ellipses, and we described how to obtain the sky background from a long-ranging series of overlapping frames.

The exposures presented are 9×300 sec in the Kron-Cousins I-band. If not stated otherwise, all magnitudes refer to the I-band. The weather was photometric and the seeing

0.″8 – 0.″9 FWHM. An additional frame of 500 sec in the Johnson V-band was used for the color term in our photometric calibration. We calibrated our frames using the standard stars in M67 (Schield 1983) and aperture photometry of our target galaxy (Burstein *et al.* 1987). The correction for Galactic absorption and K-correction equals 0.03 mag and was adopted from Goudfrooij *et al.* (1994). The statistical error of our zero point calibration is 0.03 mag. A detailed description of the basic reductions can be found in ST.

All the reductions were performed using our image handling program IMSYS. After an average bias frame and a residual bias value were subtracted the images were flat-fielded by a high signal-to-noise twilight flat, and cosmic ray events were removed. The residual flat-field errors are within 0.3% of the sky background. The residual images were obtained by subtracting a smooth fit of each image (galaxy+sky). A fit to each residual image was subtracted to account for any imperfections in the first fit. The final residual image was created by the mean of the 9 individual residuals registered to a common center. This reduces the variance of the photon noise by a factor of 9 (equivalent with an effective gain of 29.7 e^- per ADU), but does not alter the luminosity fluctuations, which are intrinsic to the galaxy. The smooth galaxy, which is used to normalize the luminosity fluctuations and photon noise, was obtained by subtracting the sky background level from one of the fits of the galaxy. The sky background level was added to the residual image, and this image was then subjected to the photometry packages and further analysis.

3. Image Analysis

3.1. Point Source Photometry

The main purpose of this work was to arrive at a reduction method which would not introduce any systematic effects due to point sources. Because the point sources appear on a background of varying amounts of luminosity and photon fluctuations due to the radial dependence of the galaxy, we subdivided the galaxy into four annuli. The annuli were: (A1) $9.''4 \leq R < 19.''4$, (A2) $19.''4 \leq R < 29.''5$, (A3) $29.''5 \leq R < 40.''2$ and (A4) $40.''2 \leq R \leq 56.''3$. The statistics of the small number of identified point sources would be affected in case the annuli were narrower.

The search for objects, the photometry and the completeness tests were made employing the photometry package DAOPHOT II (Stetson 1987). We have made a slight modification to ALLSTAR. ALLSTAR keeps an internal noise map based on the input image, the gain q in units of e^- per ADU and readout noise $\sigma^2_{\rm RON}$ in ADUs. To this we

incorporate the average galaxy flux $\bar{g}(x,y)$ and a number h, which is an estimate of the normalized amplitude of the luminosity and photon fluctuations, see below. The noise map σ^2 takes the form

$$\sigma^2(x,y) = h\,\bar{g}(x,y) + \frac{1}{q}\,r(x,y) + \sigma^2_{\rm RON}\,, \tag{1}$$

where $r(x,y)$ is the input image, i.e. the sum of the residual image with point sources and the sky background as described in Sec. 2. We thereby use a more realistic noise map of the residual image during the PSF fitting process. We estimated the normalized amplitude h of luminosity and photon fluctuations by simulations, which are described in the following. We first applied a preliminary mask and made no correction for unwanted sources. A measurement of the luminosity fluctuation power for the whole area ($9\farcs4 \leq R \leq 56\farcs3$) gave the flux $\bar{f} = 3.38$ ADU per star per 300 sec, corresponding to a magnitude $\bar{m}_I = 28.62$. Then the smooth fit of the galaxy was divided by $\bar{f}$ giving the number of stars per pixel. The number of stars per pixel was subjected to Poissonian statistics, because the discrete nature of the stars gives rise to simple counting statistics. These 'unblurred' simulated luminosity fluctuations were convolved with a PSF (not Gaussian) obtained from a fit to the Optical Transfer Function (OTF) of the PSF present in the residual image (to be described in Sec. 4), and photon noise was added. At this point we subtracted the average galaxy flux and divided by the square root of the average galaxy flux in order to obtain normalized rms fluctuations. The variance of this image of simulated SBF is the sought estimate of h. Equation (1) was then taken into account, when ALLSTAR was applied to the original residual image for creating the final mask and when applied to the star-added frames during the completeness test. The PSF used by ALLSTAR during the fitting process and by ADDSTAR as template for artificial stars, was constructed by DAOPHOT from one bright unsaturated isolated star in the residual image.

It is of importance not to misclassify statistical events like luminosity fluctuations and photon noise as real point sources, since such a misclassifying would make the correction for remaining point sources incorrect (i.e. the correction for point sources not excised by the mask). To be able to distinguish between real point sources and luminosity and photon fluctuations we simulated the latter, one image for each of the four annuli. The photometry packages were applied to the simulated fluctuations and for each annuli we determined the lower limit of SIGMA (the uncertainty of the associated magnitude as calculated by ALLSTAR) for the detection and measurement of spurious noise peaks. We then applied the photometry packages to the original residual image and forced DAOPHOT to find all objects above a threshold of 1.3 standard deviations of the sky level (as derived by DAOPHOT), thereby including both significant point sources, and spurious sources due to luminosity and photon fluctuations. The lower limit of SIGMA (as calculated by ALLSTAR) was then used to separate the luminosity fluctuations and photon noise from

the more well-determined magnitudes of the point sources in the image. In this way we were sure not to detect any luminosity or photon fluctuations as real objects, and a total of 42 point sources within the four annuli were discovered. Each point source was excised within a radius of 12 pixels from its center (for the PSF we used a radius of 25 pixels). The final mask consisted of pixel values zero (at point sources) and unity (elsewhere) and it was multiplied by a mask defining the region of interest, one for each annulus, taking the values zero (outside the annulus) and unity (inside the annulus), see Figure 1. In this way unwanted point sources were removed from the annulus of the residual image under consideration. However, globular clusters (GCs) in the faint end of NGC 3379's globular cluster system (GCS) and background galaxies would still be embedded within the luminosity fluctuations and photon noise, and this 'masking-out' of unwanted point sources would not be complete. The incompleteness of our detection procedure was tested as follows. The corrections for residual sources will be described afterwards.

3.2. Incompleteness

A total of 10021 stars (scaled PSFs) were added by ADDSTAR to the four annuli of the residual image. The range of magnitude covered 20.00 to 23.75 with bins of 0.25 mag each. To make the process of adding stars efficient we added a total of 300 stars per bin per frame and afterwards removed those which happened to be added near either another artificial star or a true stellar object. Most stars were added to the magnitude bins near the wings of equation (2) in order to improve the fit to the number of recovered stars (see below). We then reduced the frames with added stars in exactly the same way as the original frame. The completeness of our detection procedure appears in Table 1–4. In Figure 2 we show the completeness data for the four annuli. The number of recovered stars is binomially distributed, and we derived a smooth completeness curve by the method of maximum likelihood. The functional form, which turned out to give the best fit to the number of recovered stars, was

$$f(m) = \frac{1}{2}\left(1 + \left(\mathrm{erfc}(|a(m - m_{\frac{1}{2}})|^b)\right)^{\frac{1}{b}}\right) , \qquad (2)$$

Fig. 1.— The masked residual image of NGC 3379 for $9''.4 \leq R \leq 56''.3$. North is up, East is left. The normalized luminosity fluctuations correspond to a weighted mean magnitude of $\bar{m}_I = 28.67 \pm 0.04$. This is the magnitude of an object giving rise to the flux weighted mean flux $\bar{f} = 3.16$ ADU during a 300 sec exposure of NGC 3379.

where $m_{\frac{1}{2}}$ is the limiting magnitude at half probability and a is the steepness of the magnitude cutoff. The exponent b assumes a different value for the positive and negative branch of $m - m_{\frac{1}{2}}$, respectively. The incompleteness function is by definition equal to $1 - f(m)$.

We apply the photometry package DAOPHOT to both stellar point sources *and* background galaxies for mainly two reasons. Firstly, we only have to adjust one sample of photometry parameters and we are dealing with only one set of completeness functions. Secondly, if we anticipate the idea behind the power spectrum method (Sec. 4), we can justify that we do not have to treat GCs and background galaxies separately in our completeness test: The GCs in NGC 3379 are so distant that they appear stellar (i.e. not resolved), and the fraction of the GCS, which we observe, is fully determined by a completeness test involving the scaled PSFs of ADDSTAR. Because the power spectrum method uses only the information from scales of the same size as that of the PSF, the residual power from remaining GCs, *and* background galaxies, will come solely from the stellar-like core of the contributors and will be corrected for in accordance with our completeness test. The residual power from the stellar-like core of the background galaxies will therefore be corrected for, whereas any residual power on scales differing from the size of the PSF, e.g. the halo of background galaxies, are not included in the measurement of the fluctuation power.

3.3. Luminosity Functions

We regard the luminosity functions of point sources in the following way. Of foreground stars we identified one, our PSF of magnitude 15.23, and possibly two more of magnitudes 18.45 and 18.62. NGC 3379 has the galactic coordinates $(l, b) = (233\overset{\circ}{.}49, 57\overset{\circ}{.}63)$ (de Vaucouleurs *et al.* 1991) and we expect only very few foreground stars. All detected objects, apart from the three just mentioned, are fainter than 19.80. In our analysis of GCs and background galaxies we therefore only considered sources with magnitudes greater than the limit $m_0 = 19.80$.

For the globular cluster luminosity function (GCLF) we adopted a Gaussian with top point $m_{\rm GC} = 21.55 \pm 0.40$ and dispersion $\sigma = 1.4$, i.e.

Fig. 2.— Completeness function for the four annuli. For $m < 20.0$ the data are everywhere 100% complete. The limiting magnitudes at half probability $m_{\frac{1}{2}}$ are: (A1) 21.62, (A2) 21.97, (A3) 22.05, and (A4) 22.33.

$n_{GC}(m) = N_{GC} \exp\left(-(m - m_{GC})^2/2\sigma^2\right)/(2\pi\sigma^2)^{\frac{1}{2}}$, where N_{GC} is the total number of GCs per pixel. There is strong observational evidence that this is the functional form giving the best fits to GCLFs (Wing *et al.* 1995). The value of m_{GC} was based on Harris (1990) and Pritchet & van den Bergh (1985). We adopted a mean color of $B - I = 1.8$ for the GCs in NGC 3379, based on the information on the Virgo ellipticals (Couture *et al.* 1991) and a sample of Galactic GCs (Ajhar & Tonry 1994). This is in agreement with Harris (1994). The value of σ was adopted from Harris (1991). However, one may obtain an alternative value for m_{GC}. The value of $M^V_{GC} = -7.1 \pm 0.43$ (Harris 1991), the distance modulus $m - M = 30.12 \pm 0.10$ (Tonry *et al.* 1990) and a median color $V - I = 1.1 \pm 0.2$ for the GCS of NGC 3379 (Ajhar *et al.* 1994) would give $m_{GC} = 21.92$. This indefiniteness in m_{GC} introduces a systematic error in the correction for undetected GCs, which is demonstrated in Figure 3 and Figure 7. The correction for undetected GCs turned out to be much less sensitive to the adopted dispersion σ. Changing σ from 1.4 to 1.6 left the correction unchanged.

For the luminosity function of background galaxies we adopted $n_{Gal}(m) = N_0 10^{s(m-m_0)}$, where N_0 is the number of galaxies per magnitude at $m = m_0$. The slope s of the power-law luminosity function was taken to be 0.32 (Lilly *et al.* 1991 and Steidel & Hamilton 1993). Adopting $s = 0.33$ for the slope had an insignificant influence on the correction for undetected background galaxies.

With the completeness function (one for each annulus) and the luminosity functions for GCs and background galaxies we were then able to calculate the following: 1) The variance from objects lost below the detection threshold (i.e. objects not excised by the mask). This is the correction to the fluctuation power obtained from the masked residuals. 2) The variance from detected objects (i.e. those excised by the mask, either GCs or background galaxies). As a consistency check this is compared to the decrease in fluctuation power due to the masking of the detected objects. 3) The number of detected objects, which is used to normalize the luminosity functions.

3.4. Residual Variances

Fig. 3.— The radial gradient of luminosity fluctuations. The upper curve points (*) are based on corrections with $m_{GC} = 21.55$, and the lower curve points (◇) are for $m_{GC} = 21.92$. This demonstrates the systematic error due to the indefinitness in m_{GC}. The gradients are $\Delta\bar{m}_I/\Delta \log R = -0.34 \pm 0.07$ for $m_{GC} = 21.55$ and $\Delta\bar{m}_I/\Delta \log R = -0.24 \pm 0.08$ for $m_{GC} = 21.92$. The size of the symbols corresponds to the statistical error.

In order to calculate the residual variances from undetected objects we adopt the following definitions. We have $m_1 = 23.76$, the magnitude of an object giving 1 ADU per sec for the telescope and instrument used, and we define $n_{\rm GC}$ to be the average number of detected GCs per pixel with magnitude $m \geq m_0$ and flux $f_{\rm GC} = 10^{0.4(m_1 - m_{\rm GC})}$ ADU per sec. The variance from undetected GCs per pixel (i.e. the residual power) we name $\sigma^2_{\rm GC}$, whereas we define $\Sigma^2_{\rm GC}$ to be the variance from detected GCs per pixels with $m \geq m_0$. The variances may be written as

$$\sigma^2_{\rm GC} = n_{\rm GC} f^2_{\rm GC} Q \quad \text{and} \quad \Sigma^2_{\rm GC} = n_{\rm GC} f^2_{\rm GC} P \tag{3}$$

where

$$Q \equiv 10^{0.32 \ln 10 \sigma^2} \frac{\int_{m_0}^{+\infty} \frac{(1-f(m))}{(2\pi\sigma^2)^{\frac{1}{2}}} \exp\left(-\frac{(m-m_{\rm GC}+0.8\ln 10\sigma^2)^2}{2\sigma^2}\right) dm}{\int_{m_0}^{+\infty} \frac{f(m)}{(2\pi\sigma^2)^{\frac{1}{2}}} \exp\left(-\frac{(m-m_{\rm GC})^2}{2\sigma^2}\right) dm} \tag{4}$$

and

$$P \equiv 10^{0.32 \ln 10 \sigma^2} \frac{\int_{m_0}^{+\infty} \frac{f(m)}{(2\pi\sigma^2)^{\frac{1}{2}}} \exp\left(-\frac{(m-m_{\rm GC}+0.8\ln 10\sigma^2)^2}{2\sigma^2}\right) dm}{\int_{m_0}^{+\infty} \frac{f(m)}{(2\pi\sigma^2)^{\frac{1}{2}}} \exp\left(-\frac{(m-m_{\rm GC})^2}{2\sigma^2}\right) dm} \, . \tag{5}$$

These equations include normalization of the GCLF. The number of detected GCs is

$$n_{\rm GC} = \int_{m_0}^{+\infty} f(m) n_{\rm GC}(m) dm = N_{\rm GC} \int_{m_0}^{+\infty} \frac{f(m)}{(2\pi\sigma^2)^{\frac{1}{2}}} \exp\left(-\frac{(m-m_{\rm GC})^2}{2\sigma^2}\right) dm \, . \tag{6}$$

NGC 3379 is sparsely populated by GCs and, as we have detected only about a fourth of the population, we will not try to make any constraints on the I-band GCLF of NGC 3379. On the other hand, having access to all the star-added frames we are able to comment on the systematic effect on the measured magnitudes, which turns up at the faintest levels (see e.g. Harris *et al.* 1991) and affects the photometry of a GCS. The effect is seen as the difference between the true magnitude of the added artificial stars and the magnitude of the recovered stars measured by ALLSTAR. Harris *et al.* (1991) stated that the effect may be due to the fact that the faint stars identified by FIND statistically tend to be sitting on brighter than average noise fluctuations, or that the effect could be due to the routines PHOT and NSTAR, which may not measure the correct sky level. We apply ALLSTAR, which recalculates a measure of the sky level during its iterative PSF fitting process, and we believe that the bias seen in Figure 4 is caused by FIND, due to the raised probability of identifying faint objects situated upon luminosity fluctuations. In Figure 4 we have plotted the median of $m_{\rm ADDSTAR} - m_{\rm ALLSTAR}$ for each magnitude bin and indicated the scatter of each point by its Mean Absolute Deviation (MAD). The bias effect is seen to decrease with distance from the galaxy center due to the decrease in the luminosity and

photon fluctuations of the galaxy. The systematic effect on the measured magnitudes at the faintest levels must be taken into account whenever a GCLF is being sampled.

For the background galaxies we arrive at the following equations

$$\sigma^2_{\rm Gal} = n_{\rm Gal} f_0^2 V \quad \text{and} \quad \Sigma^2_{\rm Gal} = n_{\rm Gal} f_0^2 U \tag{7}$$

where

$$V \equiv \frac{\int_{m_0}^{+\infty}(1-f(m))10^{(s-0.8)(m-m_0)}dm}{\int_{m_0}^{+\infty} f(m)10^{s(m-m_0)}dm} , \tag{8}$$

and

$$U \equiv \frac{\int_{m_0}^{+\infty} f(m)10^{(s-0.8)(m-m_0)}dm}{\int_{m_0}^{+\infty} f(m)10^{s(m-m_0)}dm} , \tag{9}$$

and s is the slope of the power-law luminosity function. The normalization of the power-law is made at $m = m_0$, and because $f_0^2 = 10^{0.8(m_1-m_0)}$ this choice has no influence on the evaluation of $\sigma^2_{\rm Gal}$ and $\Sigma^2_{\rm Gal}$. The variances converge in the upper limit of the integral due to the square of the flux. The lower limit of the integral of the power-law is set to m_0 and prevents a divergence of the variance $\Sigma_{\rm Gal}$ from detected background galaxies. The number of detected background galaxies is

$$n_{\rm Gal} = \int_{m_0}^{+\infty} f(m) n_{\rm Gal}(m) dm = N_0 \int_{m_0}^{+\infty} f(m) 10^{s(m-m_0)} dm , \tag{10}$$

which is used in the normalization of $\sigma^2_{\rm Gal}$ and $\Sigma^2_{\rm Gal}$. The above equations (3)–(10) involve the whole range of the (in)completeness functions, which is an improvement on the usually adopted limiting, or cutoff, magnitudes, when evaluating the residual power.

We have made the following test of consistency, where all numbers given are for an exposure time of 300 sec. For the outermost annulus ($40''.2 \leq R \leq 56''.3$) the normalized variance of the luminosity fluctuations was $\bar{f} = \tilde{\sigma}^2_{\rm L} = 3.60$ ADU per star with no corrections applied. A measure of the unmasked residuals gave 15.00 ADU per star. The decrease in fluctuations due to the masking of detected objects therefore was 11.40 ADU per star, which ought to be comparable to a combination of the calculated numbers $\tilde{\Sigma}^2_{\rm GC}$ and $\tilde{\Sigma}^2_{\rm Gal}$ derived from the above equations. We detected 14 GCs and 8 background galaxies, a total of 22 objects, in the outermost annulus. Adopting $m_{\rm GC} = 21.55$ and $m_0 = 19.8$ we find that $\tilde{\Sigma}^2_{\rm GC} = 9.6$ if all 22 objects are considered as GCs, whereas $\tilde{\Sigma}^2_{\rm Gal} = 6.3$ if all 22 objects are considered as background galaxies. Changing $m_{\rm GC}$ to 21.92 the two numbers will be

Fig. 4.— Median of $m_{\rm ADDSTAR} - m_{\rm ALLSTAR}$ from the completeness test of each annulus. Only data for which completeness $f > 0.5$ are plotted.

$\tilde{\Sigma}^2_{\rm GC} = 7.2$ and $\tilde{\Sigma}^2_{\rm Gal} = 5.6$. If a brighter value of m_0 is adopted, $m_0 = 19.4$ (this expresses the uncertainty in m_0), we then find $\tilde{\Sigma}^2_{\rm GC} = 14.5$ and $\tilde{\Sigma}^2_{\rm Gal} = 9.7$ for $m_{\rm GC} = 21.55$, and $\tilde{\Sigma}^2_{\rm GC} = 10.5$ and $\tilde{\Sigma}^2_{\rm Gal} = 8.5$ with $m_{\rm GC} = 21.92$. All values of $\tilde{\Sigma}^2_{\rm GC}$ and $\tilde{\Sigma}^2_{\rm Gal}$ are close to the estimate 11.4 ADU per star for the luminosity fluctuations from detected objects, whereas there seems to be a tendency that the main contribution to detected objects is from GCs. This is not in agreement with Simard & Pritchet (1994). They found that a pure galaxy luminosity function was a better representation of the point sources.

The main uncertainty in the calculations above was introduced by the rather large uncertainty in the magnitude $m_{\rm GC}$ of the top point of the GCLF. This caused the systematic error on the variance from remaining GCs. The classification of the $n_{\rm GC}$ GCs and the $n_{\rm Gal}$ background galaxies was performed by the program CLASSIFY (Harris *et al.* 1991). CLASSIFY calculates an isophotal magnitude $I_{\rm i}$ and two radial moments r_1 and r_{-2}, which makes it possible to distinguish between stellar and nonstellar sources. Figure 5 shows the ALLSTAR magnitude as a function of the isophotal CLASSIFY magnitude for nearly 300 artificial stars and for the point sources of NGC 3379. For a given $I_{\rm i}$, nonstellar objects scatter to fainter I and larger r_1 and r_{-2} because of their fainter cores and broader wings. Therefore, points deviating from the stellar line are probable background galaxies. The demand that nonstellar sources should deviate more than a specific amount from the stellar line for all three parameters resulted in a total of 14 nonstellar objects, i.e. background galaxies. After visual inspection this number was reduced to a total of 10 objects. Any systematic error introduced by misclassifying the small number of objects present is insignificant. The statistical error is at this point due to the relatively small numbers of detected objects. The statistical errors for GCs and background galaxies were added in quadrature and averaged for the four annuli, and we found that the error introduced by the number counting of objects amounts to 0.02 mag. As mentioned earlier we will not try to determine the I-band GCLF of NGC 3379, due to the limited number of identified GCs, 14 in the outermost annulus. The number of galaxies found per square arcmin in the outermost annulus is 6. This is close to the values inferred from Hintzen (1991) and Lilly *et al.* (1991).

Fig. 5.— ALLSTAR magnitude as a function of CLASSIFY magnitude. For a given $I_{\rm i}$, nonstellar objects scatter to fainter I, because of their fainter cores. The lower line of dots represents the simulated stellar sources. The diamonds represent the true objects within the four annuli. Also shown is the line displaced by 0.4 mag in order to separate nonstellar sources from stellar sources. Together with similar plots of r_1 and r_{-2} this results in a total of 14 nonstellar objects, which is reduced to 10 after visual inspection.

The sum of $\sigma^2_{\rm GC}$ and $\sigma^2_{\rm Gal}$ was used to correct (i.e. decrease) the fluctuations in the masked residual image derived by the power spectrum analysis.

4. Measuring SBF

In order to derive the variance of the luminosity fluctuations of NGC 3379 we carried out the remaining analysis in the spatial Fourier power spectrum. Firstly, the SBFs are, as the point sources, subjected to the effects of seeing, and therefore white noise and luminosity fluctuations will separate during a Fourier transform of the two-dimensional residual image. Secondly, the total power of the residual image is directly related to the total power of its Fourier transform by Parcevals' Theorem. Normalization of the luminosity fluctuations may be carried out either by dividing the residual image by the square root of the average galaxy flux per pixel before doing the Fourier transform, or by dividing the power spectrum of the residual image by the average galaxy flux per pixel of the annulus under consideration, both of which give the same result. The variance of the luminosity fluctuations was obtained by applying a filtering technique to the power spectrum of the residual image. The filtering technique will be described in the following.

With the number of stars per pixel large enough to use Gaussian rather than Poissonian statistics it may be assumed that the normalized luminosity fluctuations $f(x,y)$ within the image can be described as independent Normal distributions, each with zero mean and variance $\tilde{\sigma}^2_{\rm L} = \sigma^2_{\rm L}/\bar{g}$, which we want to estimate. The window function (i.e. the mask) introduces a correlation between the real and the imaginary part of $F(u,v)$, the Fourier transform of $f(x,y)$. However, since the scale of the window function is much larger than the scale of the PSF, the effect of the window function is seen only at very low wavenumbers. On the assumption that the two components of $F(u,v)$ are independent Normal distributions, it may be shown that the power $|F(u,v)|^2$ has the Exponential distribution with parameter $\bar{g}/\sigma^2_{\rm L}$ (Hoel *et al.* 1971). Taking into account the Optical Transfer Function $OTF(u,v)$ of the PSF and the Fourier transform $N(u,v)$ of white noise, we may describe the Fourier transform of the normalized residual image by $R(u,v)$, where

$$R(u,v) = F(u,v)\,OTF(u,v) + N(u,v)\,. \tag{11}$$

We have omitted the convolution of $OTF(u,v)$ with the Fourier transform of the window function, since it is very nearly identical to $OTF(u,v)$. Normalization of the Fourier transform is made in the usual way. The mean and the variance of the power spectrum $|R(u,v)|^2$ are

$$\mathrm{Mean}(|R(u,v)|^2) = P_0\,|OTF(u,v)|^2 + P_1 \tag{12}$$

and

$$\mathrm{Var}(|R(u,v)|^2) = P_0^2\,|OTF(u,v)|^4 + P_1^2\,, \tag{13}$$

where $P_0 = \tilde{\sigma}_0^2 = \sigma_0^2/\bar{g}$ and $P_1 = \tilde{\sigma}_N^2 = \sigma_N^2/\bar{g}$. Note, $\tilde{\sigma}_0^2$ contains a contribution from faint objects that have not been excised by the window function. The $OTF(u,v)$ was dealt with in the following way. The form of the OTF adopted from Thomsen & Frandsen (1983) was

$$\begin{aligned} OTF(u,v) &= a\,H(\omega)\,\exp(-2\pi\mathrm{i}\theta) \\ \theta &= \alpha\,u + \beta\,v \\ H(\omega) &= \exp(-(\omega/\gamma)^n) \\ \omega^2 &= u^2 + v^2 + a_2\,(u^2 - v^2) + 2\,b_2\,u\,v\,, \end{aligned} \tag{14}$$

where $OTF(0,0) \equiv 1$. Saglia *et al.* (1993) have found this functional form to give one of the best fits to stellar profiles. The fit to the Fourier transform of our PSF star gave a, α, β, γ, n, a_2 and b_2, and from this set of parameters we computed the noise free $|OTF(u,v)|^2$. It should be noted that we found $n = 1.64$ which differs from the Gaussian $n = 2$. The exact location of the PSF star in the image domain is given by (α,β), and (a_2, b_2) indicate the size of any possible ellipticity as well as the direction of the ellipticity. The ellipticity of the OTF also governed the appearance of the complex Fourier transform of the luminosity fluctuations, and we took this asymmetry into account when we calculated radial profiles of average pixel values in the power spectra within elliptical rings of width 1 pixel. We thereby obtained profiles $P(\omega)$, one for each annulus in the spatial domain, and $|OTF(\omega)|^2$, as a function of the radial wave number coordinate ω. The signal in the power spectrum of the luminosity fluctuations must be given highest weight where the variance of the signal (i.e., the variance of the variance) is lowest. This leads to the low-pass filter $|OTF(\omega)|^4/(|OTF(\omega)|^4 + P_1^2/P_0^2)$. When this low-pass filter was applied to the power spectrum of the residual image, from which had been subtracted the white noise P_1 and divided by $|OTF(\omega)|^2$, we obtained an iterative procedure, arriving at the estimate of P_0:

$$P_0 = \frac{\sum_\omega nop(\omega)\,\dfrac{|OTF(\omega)|^4}{|OTF(\omega)|^4 + P_1^2/P_0^2}\,(P(\omega) - P_1)/|OTF(\omega)|^2}{\sum_\omega nop(\omega)\,\dfrac{|OTF(\omega)|^4}{|OTF(\omega)|^4 + P_1^2/P_0^2}}\,, \tag{15}$$

where $nop(\omega)$ is the number of pixels in each ring at wave number ω. The denominator is simply the normalization factor of the filter. The filter was applied to wave numbers

$30 \leq \omega \leq 90$ for which $(P(\omega) - P_1)/|OTF(\omega)|^2$ was approximately constant. Only 3–5 iterations were needed before convergence.

The power spectra of the four spatial regions are shown in Figure 6. The uncorrected power P_0 and the level of white noise P_1 measured in ADUs per 300 sec are given in Table 5. The value of P_1, which increases with increasing distance due to the decreasing galaxy background, is within a few percent from the values obtained by equation (17) of Tonry & Schneider (1988). The residual power is $P_{\rm r} = \tilde{\sigma}^2_{\rm GC} + \tilde{\sigma}^2_{\rm Gal}$. The fluctuation power $P_{\rm L} = \tilde{\sigma}^2_{\rm L}$ was obtained by subtracting $P_{\rm r}$ from the uncorrected value of P_0, and $P_{\rm L}$ is expressed as the magnitude $\bar{m}_I \pm 0.04$. The total statistical error of $\bar{m}_I$ was obtained by adding in quadrature 0.03 mag from the zero point determination, 0.01 mag from the filtering in the power spectrum, and 0.02 mag from the number counts of GCs and background galaxies.

5. Discussion

5.1. Results of SBF in NGC 3379

In ST we presented the I-band profile of NGC 3379. After a degradation this was compared with the B-band profile of Capaccioli *et al.* (1990). We thereby obtained a color gradient of $\Delta(B-I)/\Delta \log R = -0.15 \pm 0.02$. In Table 5 values of $B-I$ are given as a function of the geometric mean distance R for each annuli, together with the surface brightness of the galaxy and results from the power spectrum analysis.

Figure 3 shows the fluctuation magnitude $\bar{m}_I$ as a function of the distance R with corrections applied according to the residual power $P_{\rm r}$ for $m_{\rm GC} = 21.55$ and for $m_{\rm GC} = 21.92$. If instead we plot $\bar{m}_I$ as a function of $B-I$, we obtain Figure 7. Expressed as a function of radius the gradients are $\Delta\bar{m}_I/\Delta \log R = -0.34 \pm 0.07$ for $m_{\rm GC} = 21.55$ and $\Delta\bar{m}_I/\Delta \log R = -0.24 \pm 0.08$ for $m_{\rm GC} = 21.92$, or expressed as a function of color $\Delta\bar{m}_I/\Delta(B-I) = 2.2 \pm 0.5$ and $\Delta\bar{m}_I/\Delta(B-I) = 1.5 \pm 0.5$ respectively. The values of the gradients are based on a linear fit to the four points having different weights. The estimated measurement error for each point is dominated by the number counting of

Fig. 6.— Power spectra of the four masked annuli in the residual image (ADU per 300 sec). The power of the Optical Transfer Function $|OTF(\omega)|^2$ and the level of white noise P_1 are indicated. Also indicated is the sum of the power P_0 times $|OTF(\omega)|^2$ plus the level of white noise. For the innermost annulus the large scale structures have been depressed by the galaxy fitting routine, which very effectively fits the innermost structures of the galaxy.

detected objects. We find $\chi^2 = 2.5$ for the points with $m_{\rm GC} = 21.55$ and $\chi^2 = 3.2$ for the points with $m_{\rm GC} = 21.92$ in both Figure 3 and 7. The number of degrees of freedom for the chi-square distribution equals 2. The probabilities that chi-square should exceed either 2.5 or 3.2 by accident are 29% and 21% respectively. The values of χ^2 indicate that the estimated measurement errors for the four points are adequate. Relying on these values of χ^2 we are inclined to adopt the averaged values $\Delta\bar{m}_I/\Delta \log R = -0.29 \pm 0.08$ and $\Delta\bar{m}_I/\Delta(B-I) = 1.9 \pm 0.5$. A model, which describes $\bar{m}_I$ as a constant, can be statistically rejected, since $\chi^2 = 31.1$ and $\chi^2 = 17.3$, and the probabilities that chi-square with 3 degrees of freedom should exceed those values by accident are smaller than 0.1%. The detected gradient in $\bar{m}_I$ is therefore significant. We now make a test of the hypothesis that there is a fixed fluctuation gradient different from zero. We first adopt the slope $\Delta\bar{m}_I/\Delta(V-I) \sim 3$ (Tonry 1991) which implies $\Delta\bar{m}_I/\Delta(B-I) \sim 1.7$ according to the stellar population models of Worthey (1994). If we subtract the linear dependence from our data and fit a constant then $\chi^2 = 3.9$ for the points with $m_{\rm GC} = 21.55$ and $\chi^2 = 3.3$ for the points with $m_{\rm GC} = 21.92$. The probabilities that chi-square should exceed those values by accident are 28% and 34% respectively. We then adopt the slope $\Delta\bar{m}_I/\Delta(B-I) = 2.9$, which is predicted by the stellar population models. Subtracting this linear dependence results in $\chi^2 = 5.6$ and $\chi^2 = 14.4$, and the corresponding probabilities are 13% and 0.2%. This indicates that the gradient in $\bar{m}_I$ is not as steep as that foreseen by the stellar population models of Worthey (1994) but is in agreement with the slope of the calibration found by Tonry (1991).

What causes the luminosity fluctuations to dim towards the center? The reduction procedure takes into account the radial dependence of the correction for residual power from GCs and background galaxies, and we believe that no systematic effects due to the varying detection threshold of the point sources are present. Correction for any residual flat-fielding errors would steepen the gradient, due to the fact that flat-field errors raise with the amplitude of the signal in the image. Any dust patches within the target galaxy would increase in number towards the center and raise the power of fluctuations, and any correction would steepen the observed gradient. The radial behavior of the luminosity fluctuations is most likely caused by variations in the underlying stellar population of NGC 3379, either by radial changes in metallicity or age, or both. The consequences of the gradient in $\bar{m}_I$ will be discussed in the following.

Fig. 7.— Fluctuation magnitude $\bar{m}_I$ as a function of color $B-I$. To resemble Figure 3 $B-I$ is plotted increasing to the left. The gradients are $\Delta\bar{m}_I/\Delta(B-I) = 2.2 \pm 0.5$ for $m_{\rm GC} = 21.55$ ($*$) and $\Delta\bar{m}_I/\Delta(B-I) = 1.5 \pm 0.5$ for $m_{\rm GC} = 21.92$ ($\diamond$), see text.

5.2. Stellar Population Models

Most of the integrated light from an elliptical galaxy is expected to come from giant stars. The brightest stars in a particular bandpass are fainter in metal-rich systems than in metal-poor ones (Frogel 1988), and any changes in fluctuation magnitudes are likely to be due to changes in metallicity rather than changes in age. However, the behavior of fluctuation magnitudes and colors is more complex than that, since the variance of the galaxy light is more sensitive than the mean to the brightest stars. Worthey (1993a) presented a sample of HR diagrams with isochrones of different metallicities for V, R and I. The behavior of fluctuation color $\bar{V} - \bar{I}$ as a function of metallicity was outlined as follows. For the V magnitude the upper giant branch turns over with increasing metallicity and falls below the horizontal branch. That makes $\bar{V}$ nearly constant as a function of metallicity due to the large number of horizontal branch stars. In contrast, the giant branch in I is falling to a less degree, which implies that $\bar{V} - \bar{I}$ will become bluer with increasing metallicity (see also Worthey 1993b and Garnavich *et al.* 1994). As in Ajhar & Tonry (1994) this must be considered when fluctuation colors are used as probes for stellar populations.

The stellar population models of Worthey (1994) (hereafter Worthey) offer a large sample of magnitudes, colors and spectral features, and also fluctuation magnitudes for a wide range of wavelengths. To clarify the dependence on metallicity and age, we have handled Worthey's tabulated model indices in a way slightly different from his. Each index may be looked at as a surface on the parameter space (log(age), [Fe/H]). The sensitivity of the index-surface to changes in age and metallicity at any given location in the parameter space is expressed by the tangent plane, i.e. the gradient vector (ΔIndex/Δ log(age), ΔIndex/Δ[Fe/H]). At 11.7 Gyr (the geometric mean of 8 and 17 Gyr) and [Fe/H] = 0.0 (solar model) the gradient of an index-surface is obtained by averaging the index over the interval of age from 8 to 17 Gyr and over the interval of [Fe/H] from -0.25 to $+0.25$. In Figure 8 we illustrate the gradient by an arrow. The ratio of the components of an arrow corresponds roughly to the sensitivity parameter in Table 6 of Worthey. Any separation of age and metallicity effects, or the lack of such, stands out more clearly in respect to other indices in this two-dimensional representation.

Figure 8 shows that the near-infrared fluctuation magnitudes $\bar{K}$ and $\bar{J}$ tend to be less sensitive to changes in age and metallicity than the other indices, but the variations

Fig. 8.— Plot of variation of indices as a function of changes in age and metallicity for a population of 11.7 Gyr and [Fe/H]=0.0. The length of the two components of an arrow expresses the sensitivity to respectively age and metallicity.

are more sensitive to metallicity than age and opposite that of the optical fluctuation magnitudes $\bar{I}$ and $\bar{V}$ and the broad-band color $B-I$. As expected H_β is mainly sensitive to age and Fe_{5270} to metallicity. The gradient of Mg_2's index-surface has nearly the same direction as that of $\bar{I}$. To separate the effects of age and metallicity the arrows of two observables should be close to being perpendicular. Figure 8 also shows that $\bar{V}-\bar{I}$ would yield relatively little information on age effects, and as for Fe_{5270} metallicity dominates the gradient. It is clear that $\bar{I}$ and $\bar{V}$, which depend mainly on metallicity, should be easily calibrated against $B-I$. The gradients of the index-surfaces, defined by the arrows in Figure 8, are very sensitive to the choice of location (for Figure 8 that was 11.7 Gyr and [Fe/H]=0.0). If we calculate the slope for $\bar{I}$ between 8 and 17 Gyr as above, but for [Fe/H] between +0.25 and +0.50, we find that the gradient flattens by a factor of ~ 1.6. $\bar{I}$'s sensitivity to both age and metallicity is reduced. It turns out that $\bar{V}-\bar{I}$ at this higher metallicity is still insensitive to age, but the sensitivity to metallicity is increased by a factor of ~ 3.8.

When the I-band fluctuation magnitude and broad-band colors are looked up in the models of Worthey, it turns out that $\Delta\bar{m}_I/\Delta(B-I) = 2.9$ and $\Delta\bar{m}_I/\Delta(V-I) = 5.3$, each having the same value whether based on a change in metallicity (around [Fe/H] = 0.0) or age (around 12 Gyr). The models of Worthey also predict $\Delta(B-I)/\Delta(V-I) = 1.8$. This, together with $\Delta\bar{m}_I/\Delta(V-I) \sim 3$ as stressed in Tonry (1991) and in Ajhar & Tonry (1994), implies that $\Delta\bar{m}_I/\Delta(B-I) \sim 1.7$. The stated slope ~ 3 of $\bar{m}_I$ versus $V-I$ was based on the gradient of $\bar{m}_I$ found for NGC 205, a comparison to M31 and M32 (all three galaxies assumed to be at the same distance), and Fornax and Eridanus galaxies (Tonry 1991). The low surface brightness galaxy NGC 205 is known to have had star formation going on for an extended period (Richer *et al.* 1984). It has a large number of dust patches and shows evidence of irregular color gradients (Freedman 1992 and Peletier 1993). The SBF color $\bar{V}-\bar{I}$ for NGC 205 is shown to become redder as the $V-I$ color becomes progressively redder at larger radii, and this is interpreted as the effects of a star burst (Ajhar & Tonry 1994). Therefore, NGC 205 may not be suitable for making constraints on the general radial behavior of $\bar{m}_I$ within normal elliptical galaxies. The studies by Faber *et al.* (1992) and Worthey *et al.* (1992) on spectral data lead to gradients in Fe_{5270} and Mg_2 for a sample of elliptical galaxies. These studies show that the trends of Fe_{5270} versus Mg_2 *within* galaxies are steeper than the relation linking the galaxy nuclei, which indicates that elliptical galaxies must be described by at least two parameters. This suggests that the internal slope $\Delta\bar{m}_I/\Delta(B-I)$ may not be expected to be the same as the one derived for individual galaxies. However, our relationship between $\bar{m}_I$ and $B-I$ for NGC 3379 matches the result for NGC 205 found by Tonry (1991). The fact that these two very different galaxies seem to follow the same slope suggests that differencies in the underlying

stellar population do not have a strong influence on the relationship between $\bar{m}_I$ and $B-I$.

Combining the gradient $\Delta\bar{m}_I/\Delta\log R = -0.29 \pm 0.08$ for NGC 3379 with the gradient $\Delta\mathrm{Mg}_2/\Delta\log R = -0.065 \pm 0.003$ found by Davies *et al.* (1993) gives $\Delta\bar{m}_I/\Delta\mathrm{Mg}_2 \sim 4.5$, which is a factor of two more shallow than predicted by the stellar population models of Worthey. Similarly, combining the gradient $\Delta\bar{m}_I/\Delta\log R = -0.29 \pm 0.08$ with the gradient $\Delta\mathrm{Fe}_{5270}/\Delta\log R = -0.63 \pm 0.11$ derived from the data in Davies *et al.* (1993) we obtain $\Delta\bar{m}_I/\Delta\mathrm{Fe}_{5270} \sim 0.5$, which is also a factor of two more shallow than predicted by Worthey. This together with the fact that the observed gradient $\Delta\bar{m}_I/\Delta(B-I) = 1.9 \pm 0.5$ for NGC 3379 is shallower than predicted by the stellar population models, may be explained by the limitations of the models as follows. A galaxy is always seen in projection, and the local stellar population is a mixture of stars with a range of metallicities. In the outer region of the galaxy we observe a relatively metal-poor population, whereas in the inner region we observe a metal-rich population mixed with a fraction of metal-poor stars. Measurements of SBF are very sensitive to the giant branch stars. Since the giant branch turns over and plummets with increasing metallicity, the observed $\bar{m}_I$ will dim to a less degree towards the metal-rich center compared with the value predicted by a single-metallicity single-age model.

Due to the blue color of GCs, the contribution from the GCS will completely vanish compared to the SBF at near-infrared wavelengths. In addition to the advantageous reduction of the contribution from the GCs at near-infrared wavelengths comes the fact that seeing improves towards longer wavelengths. Pahre & Mould (1994) presented K-band observations of SBF in NGC 3379 and 9 Virgo elliptical galaxies. Their K-band SBF measurements are uncontaminated by GCs and background galaxies, but suffer from a very small ratio $P_0/P_1 \sim 4$. The present I-band measurements provide a ratio of P_0/P_1, which is more than **10 times larger**. The high level of white noise in K is due to noise in the very bright background. For NGC 3379 they found no evidence for a radial gradient in the fluctuation magnitude $\bar{m}_K$. This result supports the shallow gradient $\Delta\bar{K}/\Delta\log R \sim 0.1$ derived from the population models (Worthey) by assuming the color gradient $\Delta(B-I)/\Delta\log R = -0.15 \pm 0.02$ (ST). However, Luppino & Tonry (1993) find a considerable gradient in the SBF of the elliptical galaxy Maffei I $\Delta\bar{K}'/\Delta\log R \sim -0.6$, which is steeper and opposite in sign compared with the gradient of NGC 3379.

5.3. SBF Distance Determination

The reliability of SBF distance measurements is based essentially on the calibration of the absolute fluctuation magnitude $\bar{M}$. A theoretical (Tonry *et al.* 1990) and empirical

(Tonry 1991) calibration have appeared (see also Ajhar & Tonry 1994) and they are plotted in Figure 2 of Worthey (1993a) together with data of his stellar population models. Of the two calibrations, the empirical one is reasonably well fitted by the models in the way that $\bar{m}_I$ dims with population color, but with a slightly different slope, as discussed earlier. The attempt to use Galactic globular clusters to place constraints on the zero point or slope of the calibration of $\bar{M}_I$ for galaxies was not successful because of the very different colors of globular clusters and galaxies (Ajhar & Tonry 1994).

Due to the complexity of the elliptical NGC 205, that particular galaxy should not be given too much weight when considering the relationship between $\bar{m}_I$ and $V - I$ for normal galaxies. The standard elliptical NGC 3379 shows a convincing and reliable behavior of $\bar{m}_I$ as a function of $B - I$, and this may be considered an advantageous improvement on the calibration of fluctuation magnitude versus color, on which the distance determinations depend crucially. The weighted mean of the fluctuation magnitudes in the four annuli is $\bar{m}_I = 28.67 \pm 0.04$, which matches within the measurement errors the result found by Tonry *et al.* (1990) $\bar{m}_I = 28.63 \pm 0.04$. For a median color of $B - I = 2.2 \pm 0.1$ found for the ellipticals in Tonry *et al.* (1990) the difference in $\bar{m}_I$ due to the indefiniteness in $m_{\rm GC}$ amounts 0.03 mag. Our comparison of the results for NGC 3379 and NGC 205 gives evidence that the relationship between $\bar{m}_I$ and $B - I$ is not seriously affected by changes in the stellar population, which is a reassurance for the SBF distance measurements. A distance determination, by observations of Cepheids in an associated spiral galaxy for instance, will tie $\bar{m}_I$ to $\bar{M}_I$ and thereby fix the zero point of the calibration. In this way a color-sequence fitting procedure in the $\bar{M}_I$ versus $B - I$ diagram will be available, and for a suitable choice of broad-band color the distance is obtained.

Our earlier discussion of the radial SBF analysis of NGC 3379 together with the work on NGC 205 (Tonry 1991) and state-of-the-art stellar population models (Worthey 1994) opens the need for testing the models against additional radial investigations. The gradient in fluctuation magnitude $\bar{m}_I$ presented in this work together with the stellar population models indicates that $\bar{m}_I$ is more sensitive to changes in the underlying stellar population than is the fluctuation color $\bar{V} - \bar{I}$ when examining the radial properties of normal elliptical galaxies. Based on our results for the $\bar{m}_I$ versus $B - I$ relation we conclude that the slope of our calibration is not significantly different from the slope of the calibration applied by Tonry (1991) for the SBF distance measurements. A sample of fluctuation gradients derived form individual galaxies should be compared with calibrations for galaxies in clusters, as they may not necessarily obey the same relationship between fluctuation magnitude and broad-band color.

We are very grateful to P. B. Stetson for accessibility to the photometry package

DAOPHOT II, and we appreciate the efforts of W. E. Harris for making CLASSIFY available to us. We wish to thank H. Kjeldsen for useful comments. MS acknowledges financial support from the University of Aarhus Faculty of Science. BT acknowledges travel support by the European Southern Observatory.

REFERENCES

Ajhar, E. A., and Tonry, J. L. 1994, ApJ, 429, 557

Ajhar, E. A., Blakeslee, J. P., and Tonry, J. L. 1994, AJ, 108, 2087

Burstein, D., Davies, R. L., Dressler, A., Faber, S. M., Stone, R. P. S., Lynden-Bell, D., Terlevich, R. J., and Wegner, G. 1987, ApJS, 64, 601

Capaccioli, M., Held, E. V., Lorenz, H., and Vietri, M. 1990, AJ, 99, 1813

Couture, J., Harris, W. E., and Allwright, J. W. B. 1991, ApJ, 372, 97

Davies, R. L., Sadler, E. M., and Peletier, R. F. 1993, MNRAS, 262, 650

Dressler, A. 1993, in Proceedings of the 9th IAP Astrophysics Meeting, eds. F. R. Bouchet and M. Lachièze-Rey, Cosmic Velocity Fields, 9

de Vaucouleurs, G., de Vaucouleurs, A., Corwin, H. G., Buta, R. J., Paturel, G., and Fouqué, P. 1991, Third Reference Catalogue of Bright Galaxies (Springer, New York)

Faber, S. M., Worthey, G., and Gonzalez, J. J. 1992, in IAU Symp. 149, eds. B. Barbuy and A. Renzini, The Stellar Population of Galaxies (Dordrecht: Kluwer), 255

Freedman, W. L. 1992, in IAU Symp. 149, eds. B. Barbuy and A. Renzini, The Stellar Population of Galaxies (Dordrecht: Kluwer), 169

Frogel, J. A. 1988, ARA&A, 26, 51

Garnavich, P. G., VandenBerg, D. A., Zurek, D. R., and Hesser, J. E. 1994, AJ, 107, 1097

Goudfrooij, P., Hansen, L., Jørgensen, H. E., Nørgaard-Nielsen, H. U., de Jong, T., van den Hoek, L. B., 1994, A&AS, 104, 179

Harris, W. E. 1990, PASP, 102, 966

———. 1991, ARA&A, 29, 543

———. 1994, private communication

Harris, W. E., Allwright, J. W. B., Pritchet, C. J., and van den Bergh, S. 1991, ApJS, 76, 115

Hintzen, P., Romanishin, W., Valdes, F. 1991, ApJ, 366, 7

Hoel, P. G., Port, S. C., and Stone, C. J. 1971, in Introduction to Probability Theory (Houghton Mifflin Company, Boston), 150

Jacoby, G. H., Branch, D., Ciardullo, R., Davies, R. L., Harris, W. E., Pierce, M. J., Pritchet, C. J., Tonry, J. L., Welch, D. L. 1992, PASP, 104, 599

Lilly, S. J., Cowie, L. L., and Gardner, J. P. 1991, ApJ, 369, 79

Luppino, G. A., and Tonry, J. L. 1993, ApJ, 410, 81

Pahre, M. A., and Mould, J. R. 1994, ApJ, 433, 567

Peletier, R. F. 1993, A&A, 271, 51

Pritchet, C. J., and van den Bergh, S. 1985, AJ, 90, 2027

Richer, H. B., Crabtree, D. R., and Pritchet, C. J. 1984, ApJ, 287, 138

Saglia, R. P., Bertschinger, E., Baggley, G., Burstein, D., Colless, M., Davies, R. L., McMahan, R. K. Jr, and Wegner, G. 1993, MNRAS, 264, 961

Schield, R. E. 1983, PASP, 95, 1021

Simard, L., and Pritchet, C. J. 1994, AJ, 107, 503

Sodemann, M., and Thomsen, B. 1994a, A&A, 292, 425 (ST)

———. 1994b, poster contribution to IAU Symp. 164, Stellar Populations, in press

Stetson, P. B. 1987, PASP, 99, 191

Steidel, C. C., and Hamilton D. 1993, AJ, 105, 2017

Thomsen, B., and Frandsen, S. 1983, AJ, 88, 789

Thomsen, B., and Sodemann, M. 1993, in ESO Conference and Workshop Proceedings 45, eds. I. J. Danziger, W. W. Zeilinger, and K. Kjär, Structure, Dynamics and Chemical Evolution of Elliptical Galaxies, 547

Tonry, J. L. 1991, ApJ, 373, L1

Tonry, J. L., and Schneider, D. P. 1988, AJ, 96, 807

Tonry, J. L., Ajhar, E. A., and Luppino, G. A. 1990, AJ, 100, 1416

Wing, D. L., Harris, G. L. H., Hanes, D. A., Harris, W. E. 1995, AJ, 109, 121

Worthey, G. 1993a, ApJ, 409, 530, erratum in 418, 947

———. 1993b, ApJ, 415, L91

———. 1994, ApJS, 95, 107 (Worthey)

Worthey, G., Faber, S. M., and Gonzalez, J. J. 1992, ApJ, 398, 69

This preprint was prepared with the AAS LaTeX macros v3.0.

Figure and Table captions for 'A Gradient in the Surface Brightness Fluctuations of NGC 3379'.

Fig. 1.—The masked residual image of NGC 3379 for $9''.4 \leq R \leq 56''.3$. North is up, East is left. The normalized luminosity fluctuations correspond to a weighted mean magnitude of $\bar{m}_I = 28.67 \pm 0.04$. This is the magnitude of an object giving rise to the flux weighted mean flux $\bar{f} = 3.16$ ADU during a 300 sec exposure of NGC 3379.

Fig. 2.—Completeness function for the four annuli. For $m < 20.0$ the data are everywhere 100% complete. The limiting magnitudes at half probability $m_{\frac{1}{2}}$ are: (A1) 21.62, (A2) 21.97, (A3) 22.05, and (A4) 22.33.

Fig. 3.—The radial gradient of luminosity fluctuations. The upper curve points ($*$) are based on corrections with $m_{\rm GC} = 21.55$, and the lower curve points ($\diamond$) are for $m_{\rm GC} = 21.92$. This demonstrates the systematic error due to the indefinitness in $m_{\rm GC}$. The gradients are $\Delta\bar{m}_I/\Delta \log R = -0.34 \pm 0.07$ for $m_{\rm GC} = 21.55$ and $\Delta\bar{m}_I/\Delta \log R = -0.24 \pm 0.08$ for $m_{\rm GC} = 21.92$. The size of the symbols corresponds to the statistical error.

Fig. 4.—Median of $m_{\rm ADDSTAR} - m_{\rm ALLSTAR}$ from the completeness test of each annulus. Only data for which completeness $f > 0.5$ are plotted.

Fig. 5.—ALLSTAR magnitude as a function of CLASSIFY magnitude. For a given $I_{\rm i}$, nonstellar objects scatter to fainter I, because of their fainter cores. The lower line of dots represents the simulated stellar sources. The diamonds represent the true objects within the four annuli. Also shown is the line displaced by 0.4 mag in order to separate nonstellar sources from stellar sources. Together with similar plots of r_1 and r_{-2} this results in a total of 14 nonstellar objects, which is reduced to 10 after visual inspection.

Fig. 6.—Power spectra of the four masked annuli in the residual image (ADU per 300 sec). The power of the Optical Transfer Function $|OTF(\omega)|^2$ and the level of white noise P_1 are indicated. Also indicated is the sum of the power P_0 times $|OTF(\omega)|^2$ plus the level of white noise. For the innermost annulus the large scale structures have been depressed by the galaxy fitting routine, which very effectively fits the innermost structures of the galaxy.

Fig. 7.—Fluctuation magnitude $\bar{m}_I$ as a function of color $B - I$. To resemble Figure 3 $B - I$ is plotted increasing to the left. The gradients are $\Delta\bar{m}_I/\Delta(B - I) = 2.2 \pm 0.5$ for $m_{\rm GC} = 21.55$ ($*$) and $\Delta\bar{m}_I/\Delta(B - I) = 1.5 \pm 0.5$ for $m_{\rm GC} = 21.92$ ($\diamond$), see text.

Fig. 8.—Plot of variation of indices as a function of changes in age and metallicity for a population of 11.7 Gyr and [Fe/H]=0.0. The length of the two components of an arrow expresses the sensitivity to respectively age and metallicity.

TABLE 1.—Completeness Function for $9''.4 \leq R < 19''.4$ (A1).

TABLE 2.—Completeness Function for $19''.4 \leq R < 29''.5$ (A2).

TABLE 3.—Completeness Function for $29''.5 \leq R < 40''.2$ (A3).

TABLE 4.—Completeness Function for $40''.2 \leq R \leq 56''.3$ (A4).

TABLE 5.—Data for Radial SBF Analysis of NGC 3379.

FIGURES 1 – 8

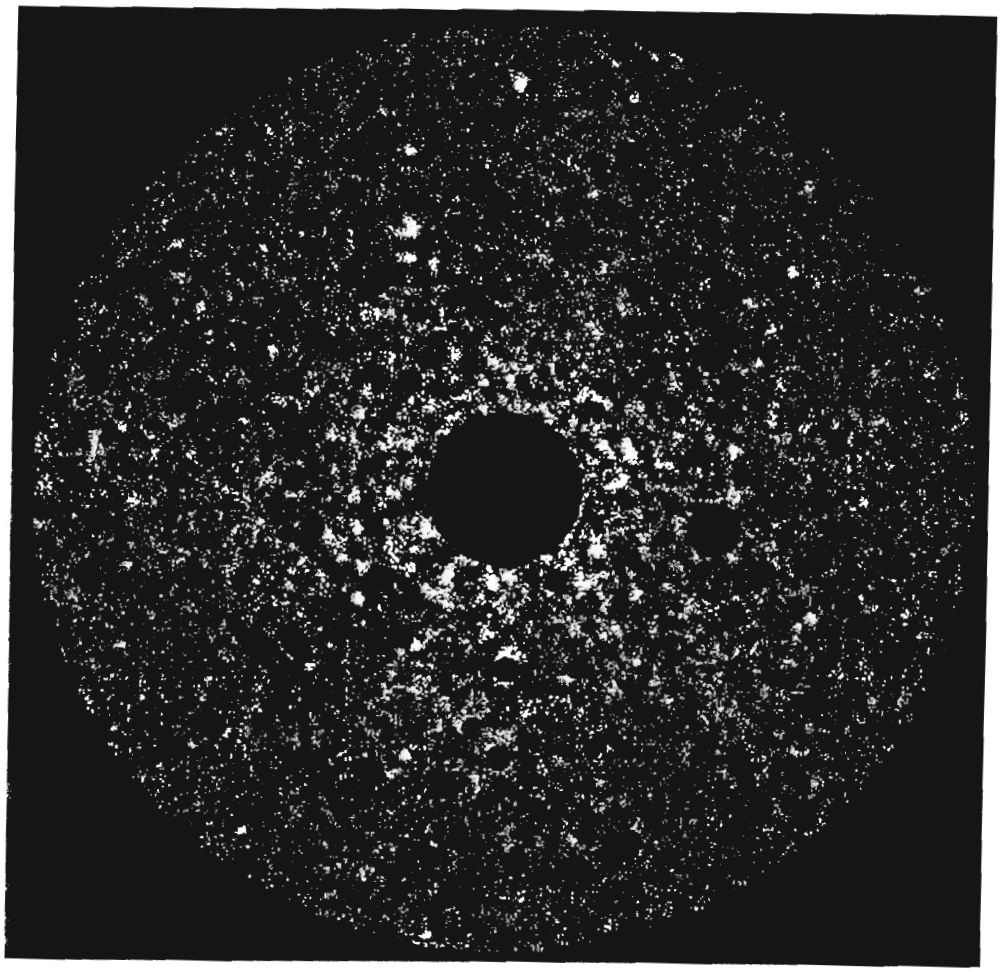

Figure 1

Figure 2

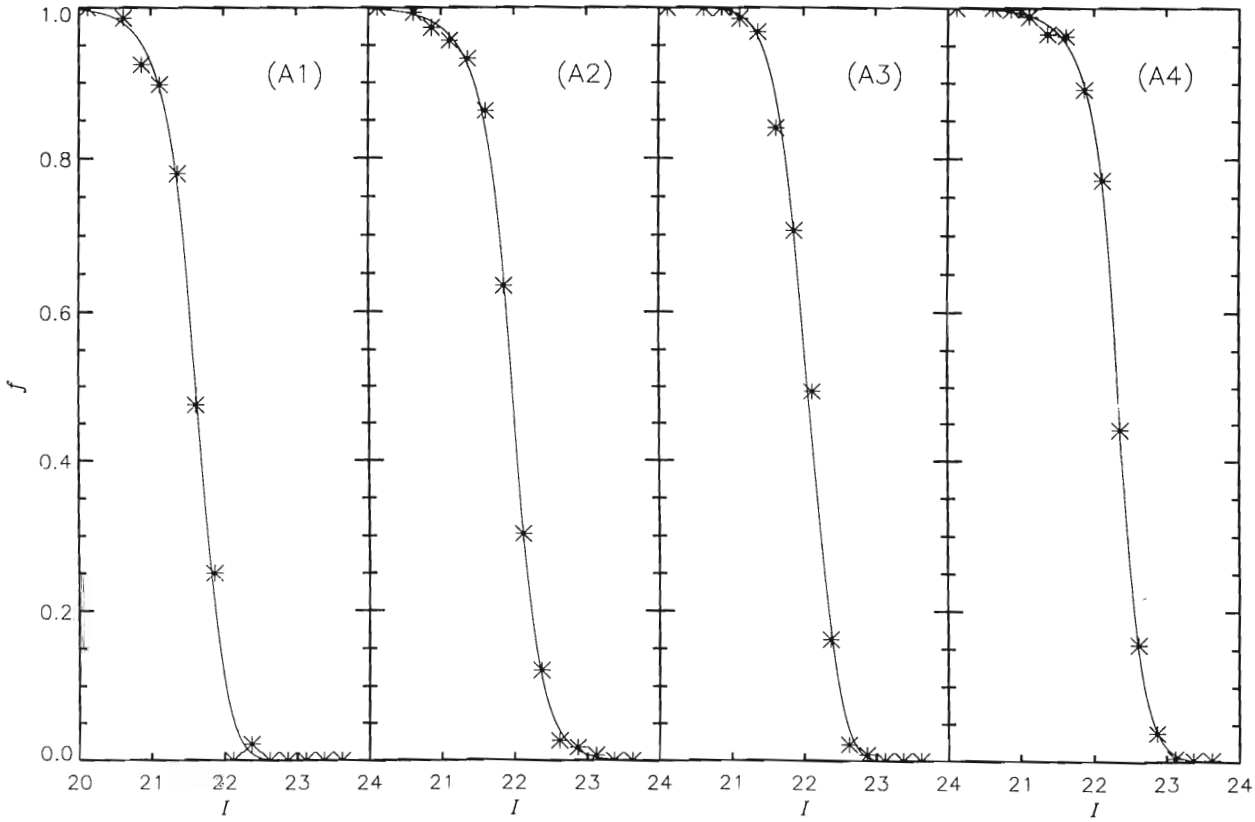

Figure 3

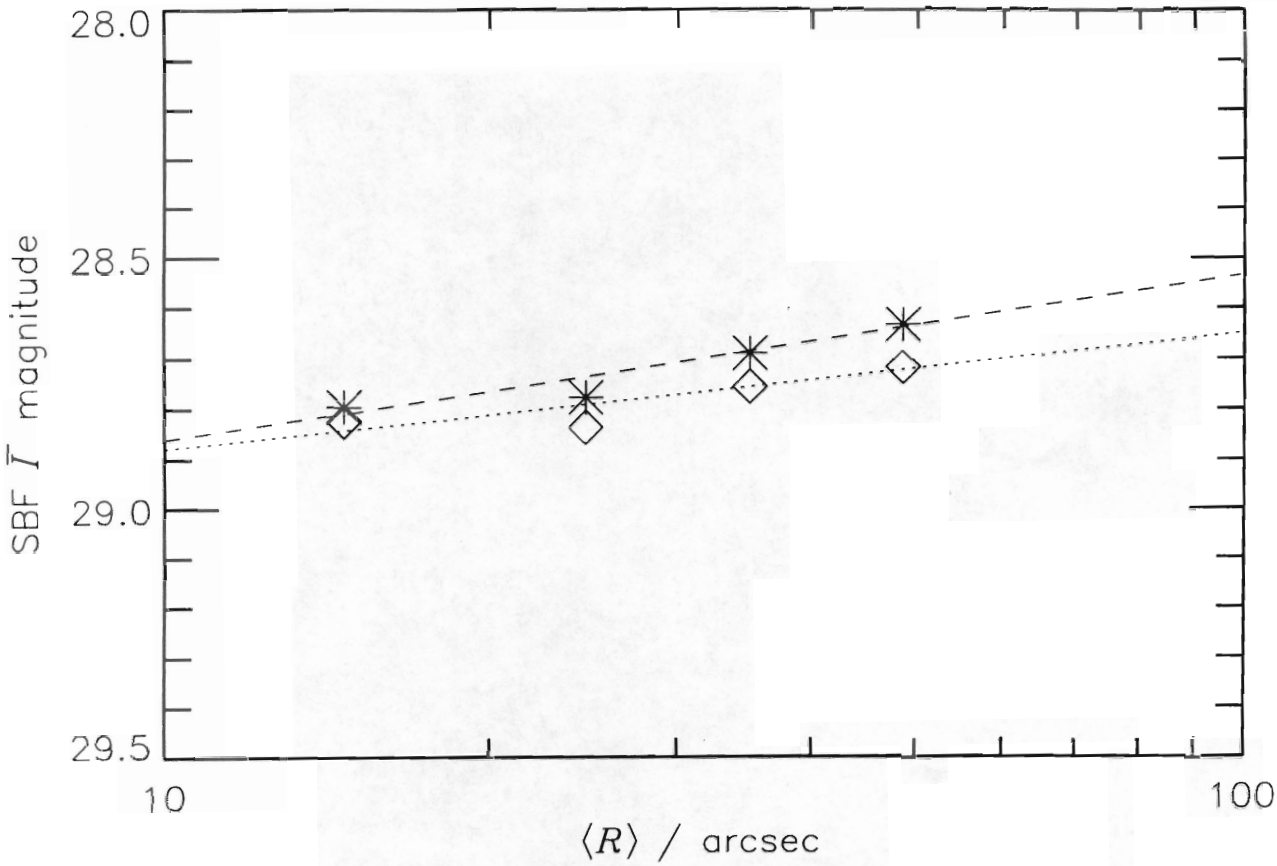

Figure 4

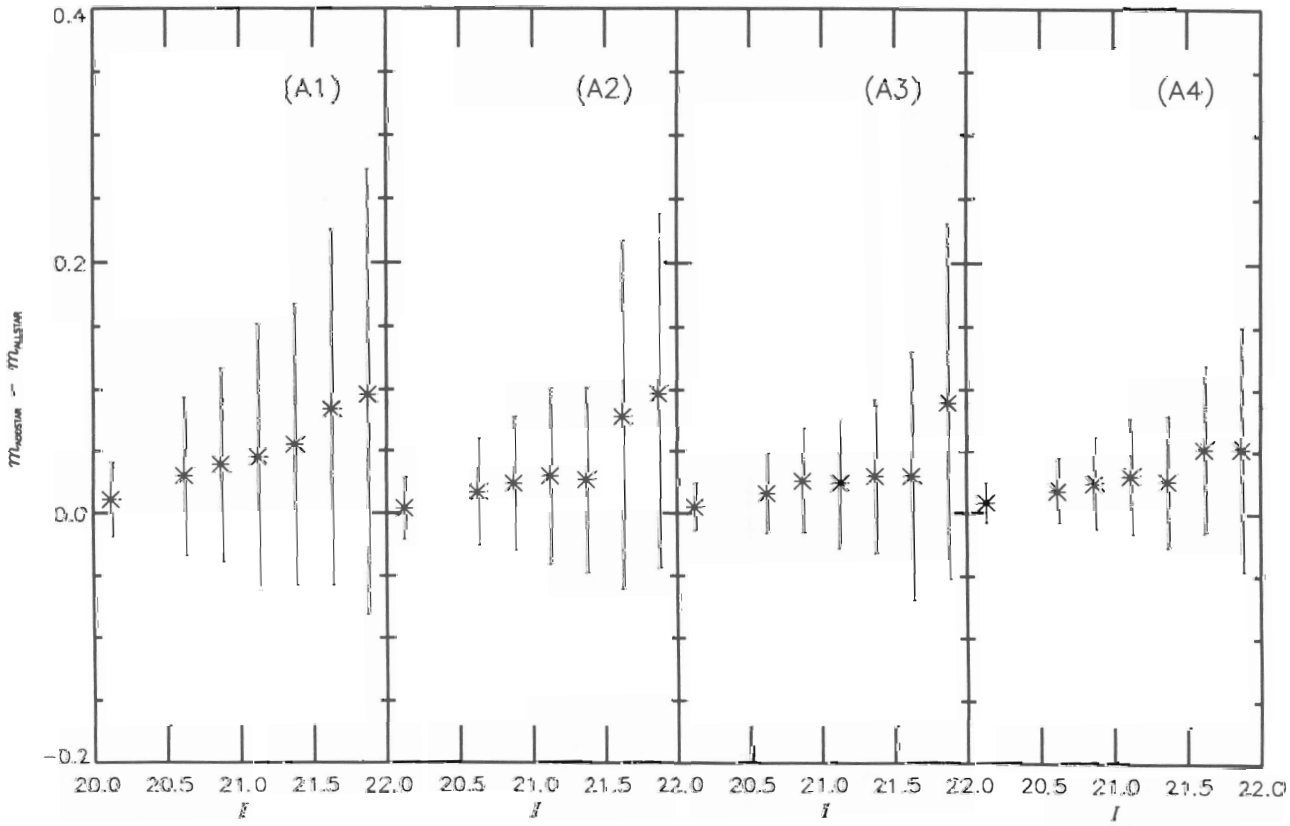

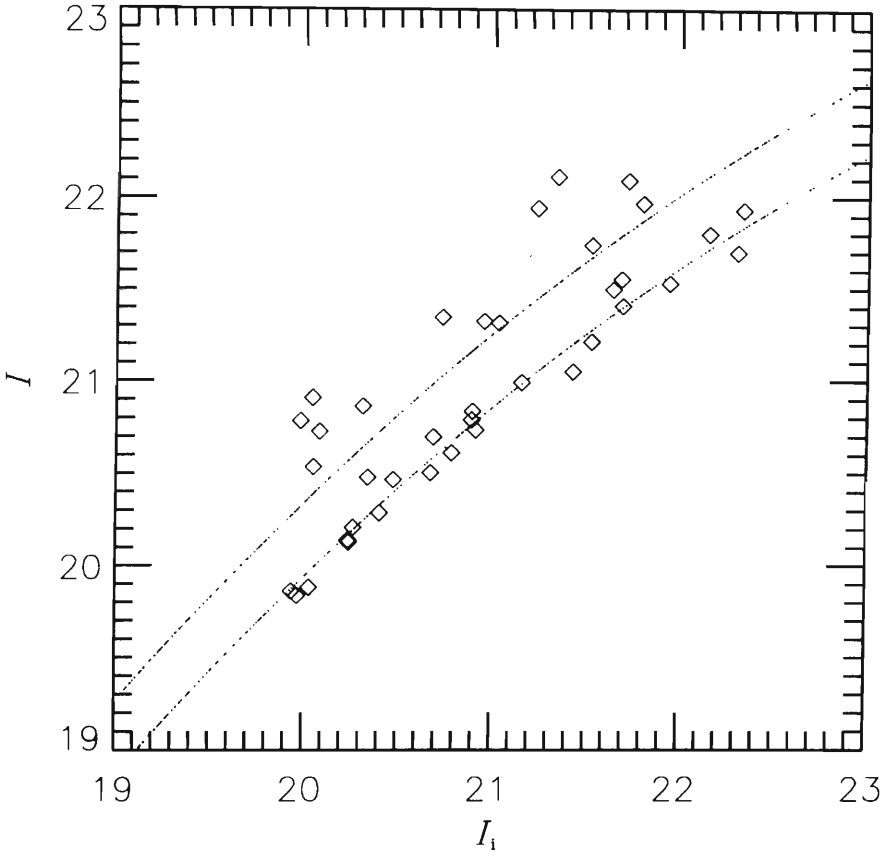

Figure 5

Figure 6

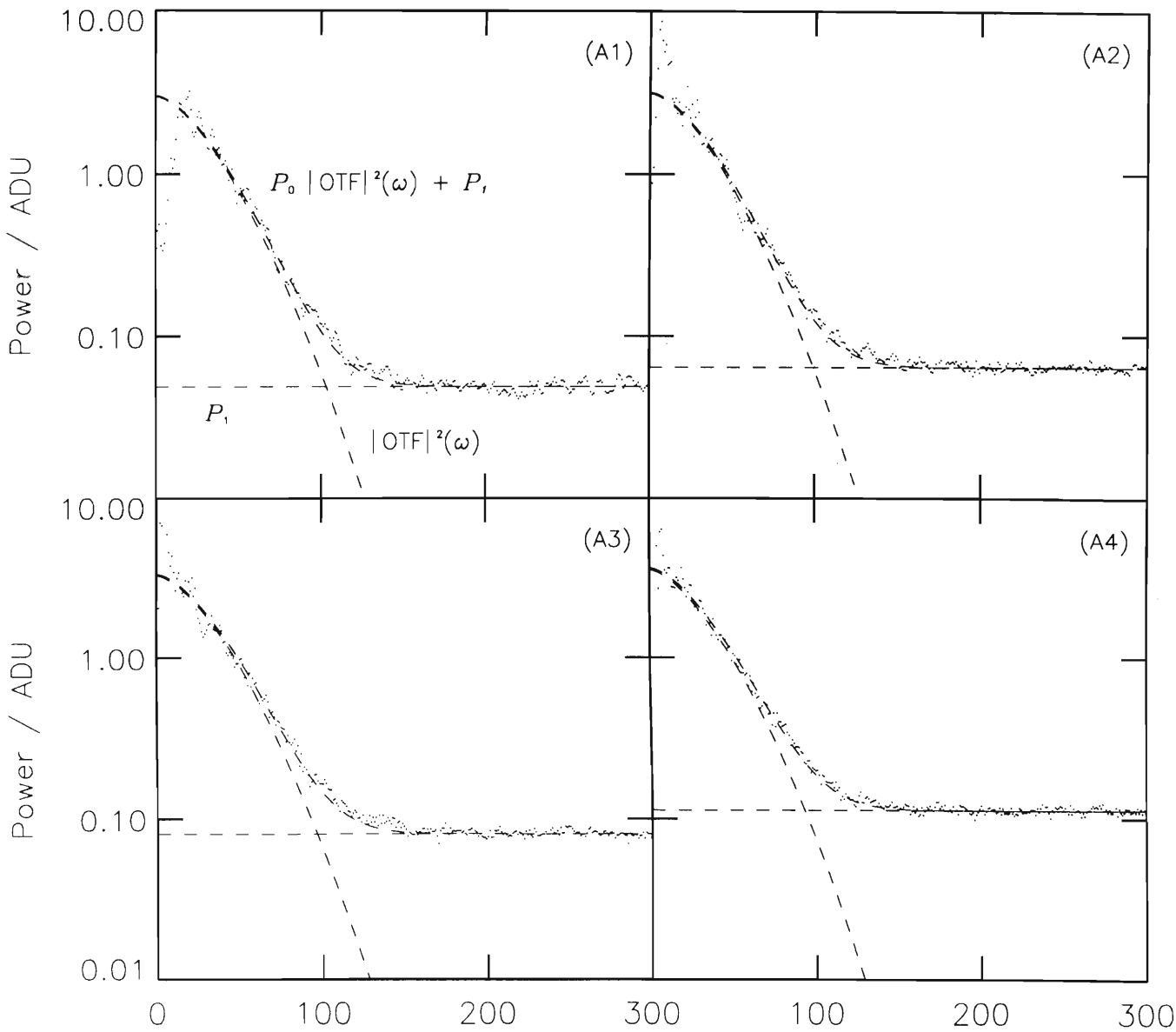

Figure 7

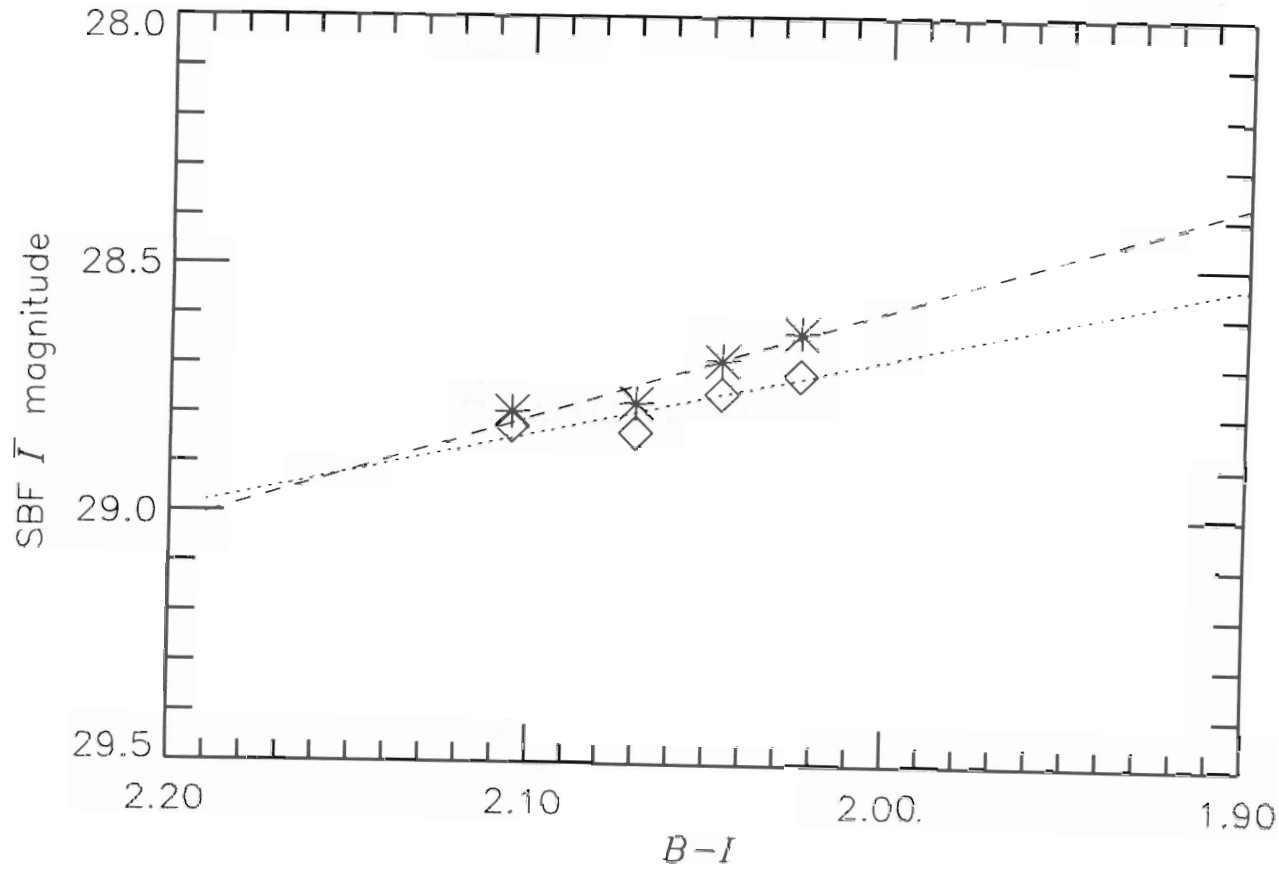

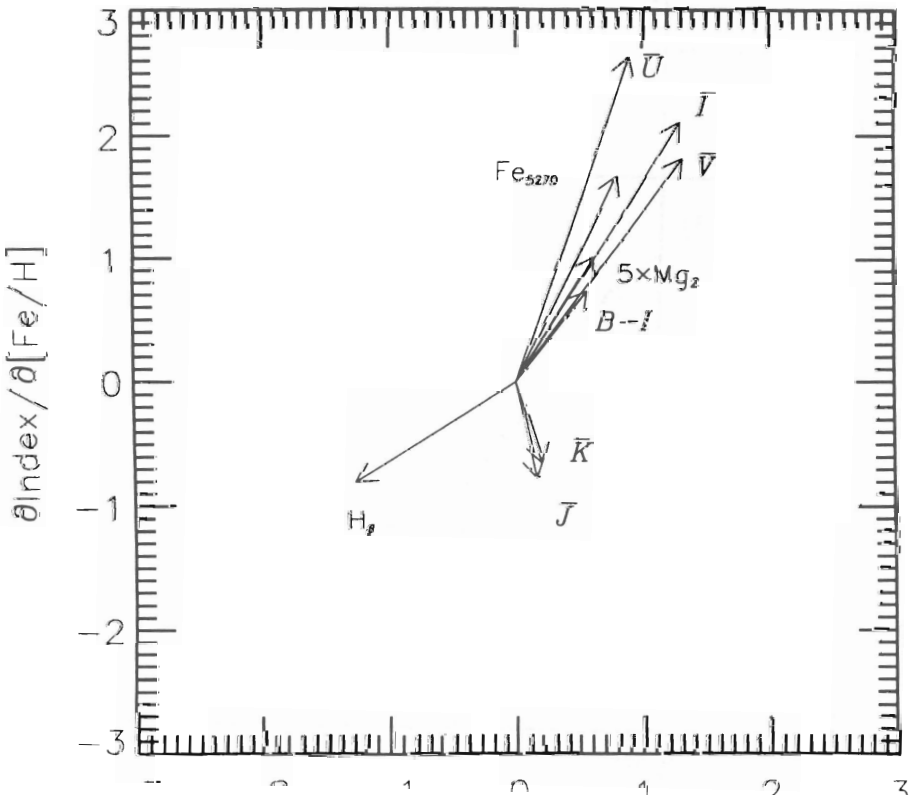

Figure 8

TABLE 1. Completeness Function for $9''.4 \leq R < 19''.4$ (A1).

I	$N_{\rm add}$	f
20.00–20.25.....	83	1.000
20.50–20.75.....	73	0.986
20.75–21.00.....	79	0.924
21.00–21.25.....	78	0.897
21.25–21.50.....	91	0.780
21.50–21.75.....	40	0.475
21.75–22.00.....	40	0.250
22.00–22.25.....	31	0.000
22.25–22.50.....	46	0.022
22.50–22.75.....	38	0.000
22.75–23.00.....	93	0.000
23.00–23.25.....	97	0.000
23.25–23.50.....	73	0.000
23.50–23.75.....	83	0.000

TABLE 2. Completeness Function for $19''.4 \leq R < 29''.5$ (A2).

I	$N_{\rm add}$	f
20.00–20.25.....	146	1.000
20.50–20.75.....	150	0.993
20.75–21.00.....	150	0.973
21.00–21.25.....	137	0.956
21.25–21.50.....	147	0.932
21.50–21.75.....	58	0.862
21.75–22.00.....	82	0.634
22.00–22.25.....	86	0.302
22.25–22.50.....	66	0.121
22.50–22.75.....	75	0.027
22.75–23.00.....	115	0.017
23.00–23.25.....	143	0.007
23.25–23.50.....	138	0.000
23.50–23.75.....	146	0.000

TABLE 3. Completeness Function for $29''.5 \leq R < 40''.2$ (A3).

I	$N_{\rm add}$	f
20.00–20.25.....	206	1.000
20.50–20.75.....	197	1.000
20.75–21.00.....	200	1.000
21.00–21.25.....	214	0.986
21.25–21.50.....	224	0.969
21.50–21.75.....	94	0.840
21.75–22.00.....	109	0.706
22.00–22.25.....	83	0.494
22.25–22.50.....	117	0.162
22.50–22.75.....	91	0.022
22.75–23.00.....	244	0.008
23.00–23.25.....	189	0.000
23.25–23.50.....	204	0.000
23.50–23.75.....	206	0.000

TABLE 4. Completeness Function for $40''.2 \leq R \leq 56''.3$ (A4).

I	$N_{\rm add}$	f
20.00–20.25.....	432	1.000
20.50–20.75.....	457	1.000
20.75–21.00.....	450	0.998
21.00–21.25.....	442	0.989
21.25–21.50.....	412	0.966
21.50–21.75.....	218	0.963
21.75–22.00.....	222	0.892
22.00–22.25.....	224	0.772
22.25–22.50.....	215	0.442
22.50–22.75.....	218	0.156
22.75–23.00.....	440	0.039
23.00–23.25.....	439	0.005
23.25–23.50.....	458	0.002
23.50–23.75.....	432	0.002

TABLE 5. Data for Radial SBF Analysis of NGC 3379.

R	μ_I	$B-I$	P_0	P_1	$\bar{m}_{\rm uncorr}$	$n_{\rm GC}$	$n_{\rm Gal}$	$n_{\rm PSF}$	$\tilde{\sigma}^2_{\rm GC}$	$\tilde{\sigma}^2_{\rm Gal}$	$P_{\rm r}$	$P_{\rm L}$	$\bar{m}_I$
14.7	17.77	2.11	2.96	0.05	28.77	2	0	0	0.07	0.00	0.07	2.89	28.80
24.6	18.77	2.07	3.09	0.06	28.73	3	2	2	0.06	0.10	0.16	2.93	28.78
35.0	19.32	2.05	3.33	0.08	28.65	10	0	1	0.15	0.00	0.15	3.18	28.69
48.5	19.89	2.02	3.60	0.11	28.56	14	8	0	0.10	0.17	0.27	3.33	28.63

Notes to Table 5.

For each annulus of the galaxy the following is tabulated. Column 1 (R) is the geometric mean of radius in arcsecs, Column 2 (μ_I) is the I-band surface brightness in magnitudes per square arcsec (ST), Column 3 ($B-I$) is the broad-band color (ST), Column 4 (P_0) and 5 (P_1) are the measured power in ADUs per 300 sec for SBF and white noise respectively, Column 6 ($\bar{m}_{\rm uncorr}$) is P_0 expressed in magnitudes, Column 7 ($n_{\rm GC}$) is the number of detected GCs, Column 8 ($n_{\rm Gal}$) is the number of detected background galaxies, Column 9 ($n_{\rm PSF}$) is the number of detected foreground stars, Column 10 ($\tilde{\sigma}^2_{\rm GC}$) and 11 ($\tilde{\sigma}^2_{\rm Gal}$) are the residual variances due to GCs and background galaxies, respectively, in ADUs per 300 sec, Column 12 ($P_{\rm r}$) is the total residual power, i.e. the sum of $\tilde{\sigma}^2_{\rm GC}$ and $\tilde{\sigma}^2_{\rm Gal}$, Column 13 ($P_{\rm L}$) is the corrected SBF power in ADUs per 300 sec, and Column 14 ($\bar{m}_I$) is $P_{\rm L}$ expressed in magnitudes. The residual variance $\tilde{\sigma}^2_{\rm GC}$ was calculated for $m_{\rm GC} = 21.55$.